Non-linear Observers for GNSS- and Camera-Aided Inertial Navigation of a Fixed-Wing UAV

Lorenzo Fusini, Thor I. Fossen, *Fellow, IEEE*, and Tor Arne Johansen, *Senior Member, IEEE*

Abstract—In this paper, exponentially stable non-linear observers for estimation of position, velocity, specific force, attitude and gyro bias of a fixed-wing unmanned aerial vehicle (UAV) are proposed. The sensor suite consists of an Inertial Measurement Unit (IMU), a global navigation satellite system (GNSS) receiver, a camera, an altimeter, and, possibly, auxiliary roll and pitch measurements. A first observer is designed making use of all the named sensors and is proven to be globally exponentially stable (GES). Subsequently, the auxiliary roll and pitch measurements are removed and replaced by an additional feedback loop from the estimated attitude, and the new observer is analysed and proven to be uniformly locally exponentially stable (ULES). An optical flow algorithm is used to calculate the UAV velocity based on the camera images, which is used as a measurement of the body-fixed velocity in the attitude observer. The performance of the observers is tested offline on simulated and experimental data.

Index Terms—navigation, nonlinear filters, unmanned aerial vehicles, optical flow.

I. Introduction

THE most used algorithm in navigation has been the Extended Kalman Filter (EKF), but in the last decades researchers have started to investigate alternatives to the EKF, namely by developing non-linear observers with stability proofs and experimental validation. Non-linear observers have the advantage, over the EKF, of featuring a smaller computational footprint and often being proven exponentially stable with a large region of attraction, a result that renders the observers robust to disturbances and initialization uncertainties. The problem of attitude estimation has received significant attention as a stand-alone problem [1]–[13]. In addition to this, researchers have integrated Inertial Navigation System (INS), magnetometer/compass, and GNSS to estimate the navigation states of a vehicle.

In [14] the author expanded the vector-based observer proposed by [8] and [9] to include GNSS velocity measurements. [1] and [2] built GES attitude estimators based on multiple time-varying reference vectors or a single persistently exiting vector. A similar observer was developed in [15] and [16] to include also gyro bias and GNSS integration. A variation of this [17] replaced the rotation matrix with the unit quaternion for representing attitude, considered Earth rotation and curvature, a non-constant gravity vector, and included accelerometer bias estimation.

Another sensor commonly used in navigation is the camera. Low weight, low power consumption, and a wide range of

Lorenzo Fusini (corresponding author), Thor I. Fossen and Tor Arne Johansen are with the NTNU Centre for Autonomous Marine Operations and Systems, Dept. of Engineering Cybernetics at the Norwegian University of Science and Technology, NO-7491 Trondheim, Norway. E-mail: {lorenzo.fusini, tor.arne.johansen}@itk.ntnu.no, thor.fossen@ntnu.no

machine vision software make it a viable choice for navigation purposes. Some drawbacks are its dependence on light and weather conditions and the difficulty in separating camera motion from moving objects in complex non-stationary environments.

Optical flow (OF) is the motion of features in the image plane between two consecutive images. Several methods exist for determining the OF of a series of images, e.g. [18]–[21]. A comparison of the performance of different methods of estimating the attitude of UAV based on machine vision is presented in [22], and different OF algorithms are evaluated in [23], [24] by estimating the UAV velocity.

The authors of the present paper have previously used OF vectors from a single camera to calculate the normalized body-fixed velocity of the UAV, which was fed into the non-linear observer as a reference vector [25]; the observer was then successfully tested on experimental data in [26]. In [27], OF was used in combination with epipolar geometry and compared with the results of [26].

A. Contributions

This paper is built on the authors' previous works [25]–[27], [28], [16], and proposes exponentially stable non-linear observers for the estimation of position, velocity, specific force, attitude, and gyro bias of a fixed-wing UAV. Exponential stability is important for systems that are exposed to environmental disturbances, measurement noise, and uncertain initialization, since it guarantees strong convergence and robustness properties [29]. Moreover, a globally stable observer has the advantage of not requiring assumptions on the characteristics of the process and measurement noise. This, together with the fact that non-linear observers have a small computational footprint, constitutes an advantage over other popular algorithms, such as the EKF.

A first observer uses a GNSS receiver, an IMU, a camera, an altimeter, and auxiliary roll and pitch measurements, with a structure that reflects the one in [15] but without using magnetometers, and is proven to be GES. Subsequently, the roll and pitch measurements are replaced by the feedback from the estimated attitude: the modified observer is then proven to be ULES. Not having to rely on roll and pitch measurements is an advantage: the sensors typically employed to obtain such angles suffer from inaccuracies in systems with fast dynamics, like fixed-wing UAVs, therefore the solution presented here has a wider range of applicability, for it obtains the roll and pitch angles from the estimated attitude.

Machine vision is implemented in order to provide the OF to the observers. The idea behind this is to find a replacement

for magnetometers: even though they are commonly used on payloads, they suffer from high and variable levels of disturbances and require an often complicated calibration procedure before use. To the best of the authors' knowledge, [25] was the first time that OF was used in a non-linear observer for navigation purposes.

The observers are tested on experimental data to corroborate the theoretical results. A computer simulation is also run to compare the observers during sharper turns of the UAV, and to demonstrate that in such cases the version with feedback from the estimated attitude performs better than the version with roll and pitch measurements.

II. NOTATION AND PRELIMINARIES

Vectors and matrices are represented by lowercase and uppercase letters, respectively. X^{-1}, X^+, and $\text{tr}(X)$ denote the inverse, pseudo-inverse, and trace of a matrix, respectively, and X^T the transpose of a matrix or vector. An estimated value of x is represented as $\hat{x}$ and the estimation error is defined as $\tilde{x} = x - \hat{x}$; similarly, for a matrix, $\tilde{X} = X - \hat{X}$. The operator $\| \cdot \|$ denotes the Euclidean norm for vectors and the Frobenius norm for matrices, I_n is the identity matrix of order n, and $0_{m \times n}$ is the $m \times n$ matrix of zeros. A vector $x = [x_1, x_2, x_3]^T$ is represented in homogeneous coordinates as $\underline{x} = [x_1, x_2, x_3, 1]^T$. The function $\text{sat}(\cdot)$ performs a component-wise saturation of its vector or matrix argument to the interval $[-1, 1]$. The operator $S(x)$ transforms the vector x into the corresponding skew-symmetric matrix, such that $S(x)y = x \times y$. The inverse operation is denoted as $\text{vex}(\cdot)$, such that $\text{vex}(S(x)) = x$. For a square matrix A, its skew-symmetric part is represented by $\mathbb{P}_a(A) = \frac{1}{2}(A - A^T)$.

The reference frames considered in the paper are the body-fixed frame {B}, the North-East-Down (NED) frame {N} (Earth-fixed, considered inertial) and the camera frame {C}. The rotation from frame {B} to {N} is represented by the matrix $R_b^n \equiv R \in SO(3)$, where $SO(3)$ represents the Special Orthogonal group. The camera is assumed to be fixed to the body and perfectly aligned to its axes, so the camera-frame and body-frame represent the same coordinate system and can be identified by {B} alone.

A vector decomposed in {B} and {N} has superscript ^{b} and ^{n} respectively. The body (camera) location w.r.t. {N} is described by $c^n = [c_x^n, c_y^n, c_z^n]^T$. A point in the environment expressed w.r.t. {N} is $t^n = [x^n, y^n, z^n]^T$: note that a point located at the mean sea level corresponds to $z^n = 0$, and such it will be considered throughout the paper. The same point expressed w.r.t. {B} is $t^b = [x^b, y^b, z^b]^T$. It will also be assumed that every point is fixed w.r.t. {N}. The gravity vector is defined as $g^n = [0, 0, g]$, with g the local gravitational acceleration. The greek letters ϕ, θ, and ψ represent the roll, pitch, and yaw angles respectively, defined according to the zyx convention for principal rotations [30]. A 2-D camera image has coordinates $[r, s]^T$, aligned with the y^b- and z^b-axis respectively. The derivative $[\dot{r}, \dot{s}]^T$ of the image coordinates is the optical flow (OF). Subscript $_F$ indicates a quantity evaluated by means of the OF.

A. Measurements and Observed System

The sensor suite consists of the following units:
- *GNSS receiver*: NED position p^n and velocity v^n;
- *IMU*: biased angular velocity $\omega_m^b = \omega^b + b^b$, where b^b represent the bias, and specific force f^b;
- *camera*: 2-D projections $[r, s]^T$ onto the image plane of points $[x^n, y^n, z^n]^T$ from the 3-D world;
- *altimeter*: height over ground c_z^n;
- roll ϕ and pitch θ angles measurements.

All measurements are affected by noise and errors, but only the gyro bias is explicitly reported here, for it is estimated by the proposed observer. The measured specific force f^b is also affected by a bias; although not explicitly considered when designing the observer, its effect is mitigated by pre-filtering the IMU readings, as explained in Sec. V-A.

The system to observe is described by [15]

$$\dot{R} = RS(\omega_m^b - b^b) \qquad \dot{p}^n = v^n$$
$$\dot{b}^b = 0 \qquad \dot{v}^n = f^n + g^n$$

with $f^n = R f^b$. Despite having direct access to v^n and p^n, they are also estimated by the observer, so that they become smoother signals and the observer preserves a particular structure that allows to exploit known theorems from [16]. Although the gyro bias is considered constant in the model, the proposed estimator can estimate its low-frequency components, as it will be evident in Sec. V.

The observer presented in Section III depends on velocity-over-ground measurements from the on-board camera decomposed in the body-fixed frame. It is necessary to compute the OF vectors from consecutive images before these vectors are transformed to velocity measurements. The method was already presented in [26].

All features tracked by the camera are assumed to be stationary with respect to {N}, hence the UAV's linear and angular velocities, v_F^b and ω_F^b, relative to a feature tracked by the OF algorithm, will be equal for every tracked feature at a given instant in time. Furthermore, it is assumed that the terrain is flat, such that every feature is located at the same altitude: this assumption can be restrictive for applications that cover an uneven surface, but it can be satisfactory for localized flights, depending on the elevation profile over which the UAV operates; it does, however, greatly simplify the analysis and calculations, such that it is worth to keep it and evaluate the performance in experiments, in Sec. V.

The angular and linear velocities can be computed by

$$\begin{bmatrix} v_F^b \\ \omega_F^b \end{bmatrix} = -M^+ [\dot{r}_1, \dot{s}_1, \cdots \dot{r}_k, \dot{s}_k]^T \qquad (1)$$

where each pair $[\dot{r}_j, \dot{s}_j]$, $j = 1...k$, represents the OF for an image feature, and $M \in \mathbb{R}^{2k \times 6}$ is a rectangular matrix built by stacking k sub-matrices M_j, $j = 1...k$. See [26] for more details on the method and the structure of M.

III. OBSERVER DESIGN

A. Assumptions

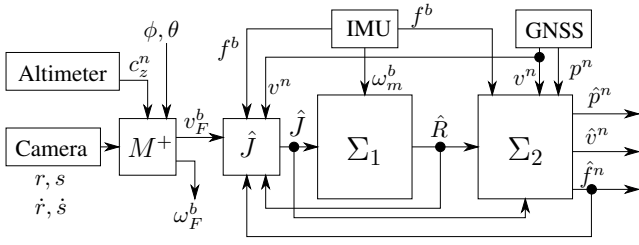When designing the non-linear observer, the following assumptions are made:

Fig. 1. Block diagram of the observer. Σ_1 represents the attitude observer, and Σ_2 the translational motion observer.

Assumption 1: A sufficient number of distinct image features are selected such that M has full rank and its pseudo-inverse can be calculated as $M^+ = (M^T M)^{-1} M^T$. Moreover, $\underline{\sigma}(M) \geq \sigma_m > 0$, where $\underline{\sigma}(M)$ is the smallest singular value of M, and σ_m a constant.

Assumption 2: The gyro bias b^b is constant, and there exists a known constant $L_b > 0$ such that $\|b^b\| \leq L_b$.

Assumption 3: There exists a constant $c_{obs} > 0$ such that, $\forall t \geq 0$, $\|f^b \times v_F^b\| \geq c_{obs}$.

Assumption 3 imposes that vectors v_F^b and f^b are non-collinear, i.e. the angle between them is non-zero and none of them can be identically zero (see, e.g., [14], [8]). This condition restricts the types of manoeuvres that ensure a correct functioning of the proposed observer. This is not an issue for fixed-wing UAVs: the specific force f^b includes the effect of gravity, implying that, for a vehicle at rest or moving at constant speed, the IMU will measure the gravitational acceleration, not zero; in addition, fixed-wing UAVs always have a positive forward velocity during flight and typically never accelerate just opposite to gravity, so that Assumption 3 is always satisfied.

B. Observer Equations

The observer is chosen as

$$\Sigma_1 \begin{cases} \dot{\hat{R}} = \hat{R}S(\omega_m^b - \hat{b}^b) + \sigma K_P \hat{J} \\ \dot{\hat{b}}^b = \text{Proj}(\hat{b}^b, -k_I \text{vex}(\mathbb{P}_a(\hat{R}_s^T K_P \hat{J}))) \end{cases} \quad (2)$$

$$\Sigma_2 \begin{cases} \dot{\hat{p}}^n = \hat{v}^n + K_{pp}(p^n - \hat{p}^n) + K_{pv}(v^n - \hat{v}^n) \\ \dot{\hat{v}}^n = \hat{f}^n + g^n + K_{vp}(p^n - \hat{p}^n) + K_{vv}(v^n - \hat{v}^n) \\ \dot{\xi} = -\sigma K_P \hat{J} f^b + K_{\xi p}(p^n - \hat{p}^n) + K_{\xi v}(v^n - \hat{v}^n) \\ \hat{f}^n = \hat{R} f^b + \xi \end{cases} \quad (3)$$

It is similar to the one in [16], but the matrix $\hat{J}$ is defined differently. The subsystem Σ_1 is the attitude observer, in which K_P is a symmetric positive definite gain matrix, $\hat{R}_s = \text{sat}(\hat{R})$, $\sigma \geq 1$ is a scaling factor tuned to achieve stability, $k_I > 0$ is a scalar gain, $\text{Proj}(\cdot, \cdot)$ represents a parameter projection that ensures that $\|\hat{b}^b\|$ not exceed a design constant $L_{\hat{b}} > L_b$ (see [15] for the definition). $\hat{J}$ is the output injection representing the attitude error, whose design is inspired by the TRIAD algorithm [31]. It is defined as

$$\hat{J}(f^b, \hat{f}^n, v_F^b, \hat{v}^n, \hat{R}) := \hat{A}_n A_b^T - \hat{R} A_b A_b^T \quad (4a)$$

$$A_b := \begin{bmatrix} f^b, & f^b \times v_F^b, & f^b \times (f^b \times v_F^b) \end{bmatrix} \quad (4b)$$

$$\hat{A}_n := \begin{bmatrix} \hat{f}^n, & \hat{f}^n \times v^n, & \hat{f}^n \times (\hat{f}^n \times v^n) \end{bmatrix} \quad (4c)$$

The body-fixed velocity vector v_F^b is calculated by means of the OF, according to

$$\begin{bmatrix} v_F^b \\ \omega_F^b \end{bmatrix} = -M^+ \begin{bmatrix} \dot{r} \\ \dot{s} \end{bmatrix} \quad (5)$$

The subsystem Σ_2 is the translational motion observer, where $K_{pp}, K_{pv}, K_{vp}, K_{vv}, K_{\xi p}$, and $K_{\xi v}$ are tunable observers gains. The estimate $\hat{f}^n$ is necessary, as it is a component of the injection term $\hat{J}$; the term ξ captures unmodelled dynamics of the specific force, and ensures the linearity of (7). The system Σ_1–Σ_2 has a feedback interconnection, as illustrated by Fig. 1.

C. Stability Analysis

The error dynamics of the attitude observer Σ_1 is

$$\dot{\tilde{R}} = RS(\omega^b) - \hat{R}S(\omega_m^b - \hat{b}^b) - \sigma K_P \hat{J} \quad (6a)$$

$$\dot{\tilde{b}}^b = -\text{Proj}(\hat{b}^b, \tau(\hat{J})) \quad (6b)$$

where $\tau(\hat{J}) = -k_I \text{vex}(\mathbb{P}_a(\hat{R}_s^T K_P \hat{J}))$. The origin of (6) was proven to be GES in [28], using magnetometers instead of optical flow, assuming that all arguments of $\hat{J}$ were perfect measurements and not estimates.

The error dynamics of Σ_2 is

$$\dot{\tilde{p}}^n = \tilde{v}^n - K_{pp} \tilde{p}^n - K_{pv} \tilde{v}^n \quad (7a)$$

$$\dot{\tilde{v}}^n = \tilde{f}^n - K_{vp} \tilde{p}^n - K_{vv} \tilde{v}^n \quad (7b)$$

$$\dot{\tilde{f}}^n = -K_{\xi p} \tilde{p}^n - K_{\xi v} \tilde{v}^n + \tilde{d} \quad (7c)$$

where $\tilde{d} = (RS(\omega^b) - \hat{R}S(\omega_m^b - \hat{b}^b))f^b + (R - \hat{R})\dot{f}^b$. By defining the error state $\tilde{w} = [(\tilde{p}^n)^T, (\tilde{v}^n)^T, (\tilde{f}^n)^T]^T$, the error dynamics (7) can be written in a more compact form as

$$\dot{\tilde{w}} = (A - KC)\tilde{w} + B\tilde{d} \quad (8)$$

where

$$A = \begin{bmatrix} 0_{6\times3} & I_6 \\ 0_{3\times3} & 0_{3\times6} \end{bmatrix}, \qquad B = \begin{bmatrix} 0_{6\times3} \\ I_3 \end{bmatrix},$$

$$C = \begin{bmatrix} I_6 & 0_{6\times3} \end{bmatrix}, \qquad K = \begin{bmatrix} K_{pp} & K_{pv} \\ K_{vp} & K_{vv} \\ K_{\xi p} & K_{\xi v} \end{bmatrix}.$$

Theorem 1: Let σ be chosen sufficiently large and define $H_K(s) = (Is - A + KC)^{-1}B$. There exists a $\gamma > 0$ such that, if K is chosen such that $A - KC$ is Hurwitz and $\|H_K(s)\|_\infty < \gamma$, then the origin of (6), (8) is GES. Moreover, K can always be chosen to satisfy these conditions.

Proof: The vectors f^b, v_F^b, and v^n in (4) are all measured or calculated using only measured quantities, whereas $\hat{f}^n$ is estimated by Σ_2. The theorem is then analogous to Theorem 3 in [16], and proof and conclusions are the same. ∎

The matrix M requires that auxiliary measurements of the roll ϕ and pitch θ angles be always available [23]. They can be measured, for example, with computations from accelerometer measurements, with inclinometers, or with a camera by using the horizon as reference [32].
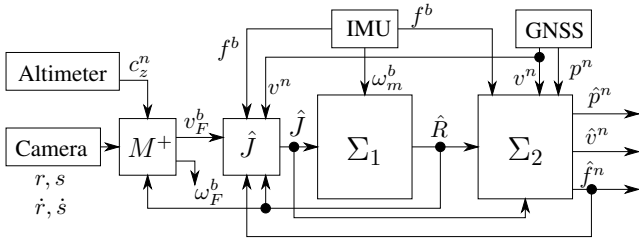
Fig. 2. Observer modified such that the roll and pitch measurements are replaced by the estimated attitude $\hat{R}$.

Roll and pitch estimates from accelerometers are often obtained statically due to the simplicity of the method, but it does not take into account the Coriolis and centripetal accelerations, leading to inaccuracies if applied to systems with fast dynamics, like UAVs. Improved performance could be obtained using a dynamic, more accurate model [30], [33].

For these reasons, it would make sense to employ the existing attitude estimate $\hat{R}$ instead of measurements.

IV. No Auxiliary Roll and Pitch Measurements

The observer presented in Sec. III estimates, among other things, the attitude of the vehicle, i.e. roll, pitch, and yaw, so it is natural to investigate whether the estimated roll and pitch can be used as an alternative to the roll and pitch measurements, as illustrated by Fig. 2.

These angles appear in M, but in the new observer they are replaced by $\hat{\phi}$ and $\hat{\theta}$, respectively, and the matrix M and its pseudo-inverse are denoted $\hat{M}$ and $\hat{M}^+$, respectively. A modified observer is presented here and proven to be ULES. In practice, local stability is not a limitation in the present case, since the global approach of Sec. III can be used, if necessary, in an initial phase until the estimation error is small, to monitor the performance of the ULES algorithm.

A. Attitude Observer with Feedback from $\hat{R}$

The analysis in Sec. III-C investigated first the stability of Σ_1 independent of Σ_2, considering all inputs measured signals. The introduction of the feedback from $\hat{R}$ makes it not possible any more to consider one of the inputs, v_F^b, a direct measurement, as it depends on $\hat{R}$ itself and is therefore renamed $\hat{v}_F^b$. It is in fact possible that the value of $\hat{R}$ be far from the actual R, for example at initialization, yielding a wrong $\hat{v}_F^b$. This means that the stability of Σ_1 has to be investigated again for this case.

In Σ_1, $\hat{J}$ now depends on $\hat{R}$ via $\hat{M}^+$, and is denoted $\bar{J}$ to avoid confusion. Assuming for the moment that all inputs except v_F^b are measurements, $\bar{J}$ is then defined as

$$\bar{J}(f^b, f^n, \hat{v}_F^b, v^n, \hat{R}) := A_n \bar{A}_b^T - \hat{R}\bar{A}_b\bar{A}_b^T \quad (9a)$$

$$\bar{A}_b := \left[f^b, \; f^b \times \hat{v}_F^b, \; f^b \times (f^b \times \hat{v}_F^b) \right] \quad (9b)$$

$$A_n := \left[f^n, \; f^n \times v^n, \; f^n \times (f^n \times v^n) \right] \quad (9c)$$

so the observer equations are written as

$$\Sigma_1' \quad \begin{cases} \dot{\hat{R}} = \hat{R}S(\omega_m^b - \hat{b}^b) + \sigma K_P \bar{J} \\ \dot{\hat{b}}^b = \text{Proj}(\hat{b}^b, -k_I \text{vex}(\mathbb{P}_a(\hat{R}_s^T K_P \bar{J}))) \end{cases} \quad (10)$$

The error dynamics is then

$$\dot{\tilde{R}} = RS(\omega^b) - \hat{R}S(\omega_m^b - \hat{b}^b) - \sigma K_P \bar{J} \quad (11a)$$

$$\dot{\tilde{b}}^b = -\text{Proj}(\hat{b}^b, \tau(\bar{J})) \quad (11b)$$

Lemma 1: Assume that $0 < c \le \|f^b\|^2 \le k_a$, for positive k_a and c. For any given choice of K_P and k_I, there exists a $\sigma^* > 0$ such that, for all $\sigma \ge \sigma^*$, the origin of (11) is ULES.

Proof: $\hat{M}$ can be written as $\hat{M} = \hat{M}_1 + M_2$, where

$$\hat{M}_1 = -\frac{1}{c_z^n}\hat{r}_{31} \begin{bmatrix} 0 & -s & \frac{rs}{l} & 0 & 0 & 0 \\ s & 0 & \frac{s^2}{l} & 0 & 0 & 0 \end{bmatrix}$$
$$+ \frac{1}{c_z^n}\hat{r}_{32} \begin{bmatrix} 0 & -r & \frac{r^2}{l} & 0 & 0 & 0 \\ r & 0 & \frac{rs}{l} & 0 & 0 & 0 \end{bmatrix}$$
$$+ \frac{1}{c_z^n}\hat{r}_{33} \begin{bmatrix} 0 & -l & r & 0 & 0 & 0 \\ l & 0 & s & 0 & 0 & 0 \end{bmatrix}$$

$$M_2 = \begin{bmatrix} 0 & 0 & 0 & -\frac{l^2+r^2}{l} & -\frac{rs}{l} & -s \\ 0 & 0 & 0 & -\frac{rs}{l} & -\frac{l^2+s^2}{l} & r \end{bmatrix} \quad (12)$$

It is evident that $\hat{M}$ is linear in $\hat{R}$, and since $\hat{r}_{ij} = r_{ij} - \tilde{r}_{ij}$, $\hat{M}$ is linear in $\tilde{R}$ as well.

A linear approximation for $\hat{M}^+$ is used, in order to render the pseudo-inverse treatable. Replacing $\hat{r}_{ij}$ with $r_{ij}-\tilde{r}_{ij}$ in $\hat{M}_1$ allows to separate the part that depends on R, called $m(R)$, from the part that depends on $\tilde{R}$, called $m(\tilde{R})$, such that $\hat{M} = m(R) - m(\tilde{R}) + M_2 = M + E$, where $E = -m(\tilde{R})$ is the error introduced with the feedback of $\hat{R}$. Since E is linear in $\tilde{R}$, a small perturbation around the origin of (6) will result in a small E. Following [34], the pseudo-inverse $\hat{M}^+$ can then be expressed using the Neumann expansion of $(\hat{M}^T \hat{M})^{-1}$ as

$$\hat{M}^+ = M^+ - M^+ E M^+ + (M^T M)^{-1} E^T (I - M M^+) + \mathcal{O}(E) \quad (13)$$

where $\mathcal{O}(E)$ contains higher-order components, and

$$\|\hat{M}^+\| \le k_M + k_E\|\tilde{R}\| + \mathcal{O}(\|\tilde{R}\|^2) \quad (14)$$

where k_M and k_E depend solely on physical quantities, hence they are bounded by Assumption 1, and $\mathcal{O}(\|\tilde{R}\|^2)$ is a remainder term containing all the powers of $\|\tilde{R}\|$ above one.

Following [28], choose the Lyapunov function candidate

$$V(\tilde{R}, \tilde{b}^b) = \frac{1}{2}\|\tilde{R}\|^2 - \ell\text{tr}(S(\tilde{b}^b)R^T\tilde{R}) + \frac{\ell\sigma}{k_I}\|\tilde{b}^b\|^2$$

which satisfies $\alpha_1(\|\tilde{R}\|^2 + \|\tilde{b}^b\|^2) \le V \le \alpha_2(\|\tilde{R}\|^2 + \|\tilde{b}^b\|^2)$. Hence,

$$\dot{V} = \text{tr}(\tilde{R}^T(\tilde{R}S(\omega^b + \tilde{b}) - RS(\tilde{b})) - \sigma\text{tr}(\tilde{R}^T K_P \bar{J})$$
$$+ \ell\text{tr}(S(\text{Proj}(\hat{b}, -k_I\text{vex}(\mathbb{P}(\hat{R}_s^T K_P \bar{J}))))R^T\tilde{R})$$
$$- \ell\text{tr}(S(\tilde{b})S^T(\omega^b)R^T\tilde{R}) - \ell\text{tr}(S(\tilde{b})R^T\tilde{R}S(\omega^b + \tilde{b}))$$
$$+ \ell\text{tr}(S(\tilde{b})R^T RS(\tilde{b})) + \ell\sigma\text{tr}(S(\tilde{b})R^T K_P \bar{J})$$
$$- \frac{2\ell\sigma}{k_I}\tilde{b}^T\text{Proj}(\hat{b}, -k_I\text{vex}(\mathbb{P}(\hat{R}_s^T K_P \bar{J})))$$

Considering that $A_n = RA_b$ and $\hat{R} = R - \tilde{R}$, it is possible to write $\bar{J} = R(A_b - \bar{A}_b)\bar{A}_b^T - \tilde{R}\bar{A}_b\bar{A}_b^T$, whose norm is $\|\bar{J}\| \le \|A_b - \bar{A}_b\|\|\bar{A}_b\| + \|\tilde{R}\|\|\bar{A}_b\|^2$. Defining $\epsilon := [0, f^b \times \tilde{v}_F^b, f^b \times$

$(f^b \times \tilde{v}_F^b)]$, it is $A_b - \bar{A}_b = \epsilon$. Since $\tilde{v}$ depends linearly on $\tilde{R}$ and when $\tilde{R} = 0$ it is $\tilde{v}_F^b = 0$ and $\epsilon = 0$, it results that $\|\epsilon\| \leq \|f^b\|\|\tilde{R}\|k$. The norm of $\bar{J}$ is then $\|\bar{J}\| \leq \|\tilde{R}\|(k\|f^b\|\|\bar{A}_b\| + \|\bar{A}_b\|^2)$. The matrix $\bar{A}_b$ has norm $\|\bar{A}_b\|^2 = \|f^b\|^2 + \|f^b \times \hat{v}_F^b\|^2 + \|f^b \times (f^b \times \hat{v}_F^b)\|^2$. Considering (5) and (14), $\hat{v}_F^b$ is bounded by $\|\hat{v}_F^b\|^2 \leq k_v(k_M + k_E\|\tilde{R}\| + \mathcal{O}(\|\tilde{R}\|^2))^2$ for some positive k_v. The matrix $\bar{A}_b$ can then be bounded by

$$\|\bar{A}_b\|^2 \leq k_1 + k_2\|\tilde{R}\| + k_3\|\tilde{R}\|^2 + \mathcal{O}(\|\tilde{R}\|^3) \qquad (15)$$

for positive k_1, k_2, and k_3. Finally, $\bar{J}$ is bounded by

$$\|\bar{J}\| \leq \beta_1\|\tilde{R}\| + \beta_2\|\tilde{R}\|^2 + \mathcal{O}(\|\tilde{R}\|^3) \qquad (16)$$

for some positive β_1 and β_2. $\dot{V}$ is bounded by

$$\begin{aligned}
\dot{V} \leq &+ \sqrt{6}\|\tilde{R}\|\|\tilde{b}\| - \sigma\lambda_m(K_P)c\|\tilde{R}\|^2 - 2\ell\|\tilde{b}\|^2 \\
&+ (3\sqrt{3}\ell k_I + \sqrt{6}\ell\sigma L_{\tilde{b}})\|K_P\|(\beta_1\|\tilde{R}\|^2 + \mathcal{O}(\|\tilde{R}\|^3)) \\
&+ 2\sqrt{3}\ell L_\omega\|\tilde{R}\|\|\tilde{b}\| + 2\sqrt{3}\ell(L_\omega + L_{\tilde{b}})\|\tilde{R}\|\|\tilde{b}\|
\end{aligned}$$

For small $\|\tilde{R}\|$ and $\|\tilde{b}\|$, the terms of order higher than two can be dominated to yield

$$\dot{V} \leq - \begin{bmatrix} \|\tilde{R}\| & \|\tilde{b}\| \end{bmatrix} \begin{bmatrix} \sigma q_1 - \ell q_2 - \sigma\ell q_3 & -q_4 - \ell q_5 \\ -q_4 - \ell q_5 & 2\ell \end{bmatrix} \begin{bmatrix} \|\tilde{R}\| \\ \|\tilde{b}\| \end{bmatrix}$$

where L_ω and $L_{\tilde{b}}$ are bounds on ω and $\tilde{b}$, respectively, and the different q_1, q_2, q_3, q_4, and q_5 are constant positive values independent of σ and ℓ. Choose ℓ independent of σ and sufficiently small such that $q_1 - \ell q_3 \geq r_1$, for some $r_1 > 0$.

The first-order principal minor of the above matrix is positive if σ is chosen to satisfy $\sigma > \ell q_2/r_1$. The second-order principal minor is positive if σ is chosen to satisfy $\sigma > ((q_4 + \ell q_5)^2 + 2\ell^2 q_2)/(2\ell r_1)$. Hence, for a sufficiently large σ there exists an $\alpha_3 > 0$ such that $\dot{V} \leq -\alpha_3(\|\tilde{R}\|^2 + \|\tilde{b}\|^2)$, which implies local exponential stability. ∎

B. Integration of the Translational Motion Observer

When connecting Σ_1' to the translational motion observer, f^n has to be replaced by $\hat{f}^n$, and it gives rise to a new matrix $\hat{\bar{J}}$ that substitutes $\bar{J}$. The complete observer equations are

$$\Sigma_1' \begin{cases} \dot{\hat{R}} = \hat{R}S(\omega_m^b - \hat{b}^b) + \sigma K_P\hat{\bar{J}} \\ \dot{\hat{b}}^b = \text{Proj}(\hat{b}^b, -k_I\text{vex}(\mathbb{P}_a(\hat{R}_s^T K_P\hat{\bar{J}}))) \end{cases} \qquad (17)$$

$$\Sigma_2' \begin{cases} \dot{\hat{p}}^n = \hat{v}^n + K_{pp}(p^n - \hat{p}^n) + K_{pv}(v^n - \hat{v}^n) \\ \dot{\hat{v}}^n = \hat{f}^n + g^n + K_{vp}(p^n - \hat{p}^n) + K_{vv}(v^n - \hat{v}^n) \\ \dot{\xi} = -\sigma K_P\hat{\bar{J}}\hat{f}^b + K_{\xi p}(p^n - \hat{p}^n) + K_{\xi v}(v^n - \hat{v}^n) \\ \hat{f}^n = \hat{R}f^b + \xi \end{cases} \qquad (18)$$

and the error dynamics is

$$\Sigma_1' \begin{cases} \dot{\tilde{R}} = RS(\omega^b) - \hat{R}S(\omega_m^b - \hat{b}^b) - \sigma K_P\hat{\bar{J}} \\ \dot{\tilde{b}}^b = -\text{Proj}(\hat{b}^b, \tau(\hat{\bar{J}})) \end{cases} \qquad (19)$$

$$\Sigma_2' \left\{ \dot{\tilde{w}} = (A - KC)\tilde{w} + B\tilde{d} \right. \qquad (20)$$

with (20) defined as in (8).

Theorem 2: Let σ be chosen to ensure stability according to Lemma 1 and define $H_K(s) = (Is - A + KC)^{-1}B$. There exists a $\gamma > 0$ such that, if K is chosen such that $A - KC$ is Hurwitz and $\|H_K(s)\|_\infty < \gamma$, then the origin of the error dynamics (20)–(19) is ULES. Moreover, a K that satisfies these conditions can always be found.

Proof: The proof proceeds in a fashion similar to Theorem 1. As (20) and (8) are identical, K can always be chosen to satisfy the conditions of the theorem. By choosing the same Lyapunov function candidate V, the same $\dot{V}$ is obtained, only with $\hat{\bar{J}}$ instead of J

$$\begin{aligned}
\dot{V} \leq &- \alpha_3(\|\tilde{R}\|^2 + \|\tilde{b}^b\|^2) + \text{tr}(\tilde{R}^T\sigma K_P\tilde{\hat{\bar{J}}}) \\
&- \ell\text{tr}(S(\text{Proj}(\hat{b}^b, \tau(\bar{J})) - \text{Proj}(\hat{b}^b, \tau(\hat{\bar{J}})))R^T\tilde{R}) \\
&- \ell\text{tr}(S(\tilde{b}^b)R^T\sigma K_P\tilde{\hat{\bar{J}}}) \\
&+ \frac{2\sigma\ell}{k_I}\tilde{b}^{bT}(\text{Proj}(\hat{b}^b, \tau(\bar{J})) - \text{Proj}(\hat{b}^b, \tau(\hat{\bar{J}})))
\end{aligned}$$

$\bar{J}$ is bounded as (16), and a bound for $\tilde{\hat{\bar{J}}} = (A_n - \hat{A}_n)\bar{A}_b^T = \tilde{A}_n\bar{A}_b^T$ has to be found. $\tilde{A}_n$ is bounded, as already seen in the proof of Theorem 1, as $\|\tilde{A}_n\| \leq h_1\|\tilde{w}\|$ for some positive h_1. The bound on $\bar{A}_b^T$ is derived from the proof of Lemma 1: given (15), it is also $\|\bar{A}_b\| \leq \sum_{i=0}^\infty \delta_i\|\tilde{R}\|^i = L(\|\tilde{R}\|)$, for some positive δ_i. The combination of these results yields $\|\tilde{\hat{\bar{J}}}\| \leq h_1\|\tilde{w}\|L(\|\tilde{R}\|)$. Neglecting the terms of order greater than two due to linearization about the origin, $\dot{V}$ becomes

$$\begin{aligned}
\dot{V} \leq &- \alpha_3(\|\tilde{R}\|^2 + \|\tilde{b}^b\|^2) \\
&+ (\sqrt{3}s_1 + \sqrt{6}\ell s_3)h_1\|\tilde{R}\|\|\tilde{w}\|L(\|\tilde{R}\|) \\
&+ (+\sqrt{6}\ell s_1 + \frac{2\sigma\ell s_3}{k_I})h_1\|\tilde{b}^b\|\|\tilde{w}\|L(\|\tilde{R}\|) \\
\leq &- \alpha_3\zeta^2 + (\sqrt{3}s_1 + \sqrt{6}\ell s_3)h_1\delta_0\|\tilde{R}\|\|\tilde{w}\| \\
&+ (\sqrt{6}\ell s_1 + \frac{2\sigma\ell s_3}{k_I})h_1\delta_0\|\tilde{b}^b\|\|\tilde{w}\| \\
\leq &- \alpha_3\zeta^2 + n\zeta\|\tilde{w}\|
\end{aligned}$$

for some $n > 0$ and $\zeta := (\|\tilde{R}\|^2 + \|\tilde{b}^b\|^2)^{1/2}$. Considering again the Lyapunov function $U = W + \gamma V$ from Theorem 1, the system results to be ULES. ∎

V. EXPERIMENTAL RESULTS

A. Setup

The UAV used is a UAV Factory Penguin-B with a custom-made payload that includes all the necessary sensors. The IMU is a Sensonor STIM300, a low-weight, tactical grade, high-performance sensor that includes gyroscopes, accelerometers, and inclinometers, all recorded at 300 Hz. The GPS receiver is a uBlox LEA-6T, which gives measurements at 5 Hz. The video camera is an IDS GigE uEye 5250CP provided with an 8mm lens. The camera is configured for a hardware-triggered capture at 10 Hz: the uBlox sends a digital pulse-per-second signal whose rising edge is accurately synchronized with the time of validity of the recorded GPS position, ensuring that the image capture is synchronized with the position measurement. The experiment has been carried out on 6 February 2015 at the Eggemoen Aviation and Technology Park, Norway, in a sunny day with good visibility, very little wind, an air temperature of about -8°C. The terrain is covered with snow and flat enough to let all features be considered lying at zero altitude.

All the images are captured with a resolution of 1600×1200 pixels and without any filtering or correction of distortion. SIFT is implemented with the open source computer vision library (OpenCV) [35] with default settings. Each match is tagged with a value indicating the accuracy of the match, and the smallest of these values is considered to be the best match. To increase the reliability of the OF vectors, each match is compared to the best one: every match with an uncertainty more than double the uncertainty of the best match is removed. Also the template matching algorithm is implemented with OpenCV. The size of the templates is chosen to be 120×90 pixels, and a correlation of 99% is required to consider a template match reliable.

The observers are implemented using forward Euler discretization with a time-varying step depending on the interval of data acquisition of the fastest sensor, namely the STIM300, typically around 0.003 seconds. All the tunable gains are obtained by running the observers several times and correcting the gains until a satisfactory performance was achieved. For all the different case studies, the parameters and gains are chosen as $L_{b^b} = 2°/\text{s}$, $L_{\hat{b}^b} = 2.1°/\text{s}$, $\sigma = 1$, $K_P = \text{diag}[0.08, 0.04, 0.06]$, $k_I = 0.02$, $K_{pp} = 30I_3$, $K_{pv} = 2I_3$, $K_{vp} = 0.01I_3$, $K_{vv} = 20I_3$, $K_{\xi p} = I_3$, and $K_{\xi v} = 50I_3$.

The reference for the position, velocity, and attitude is the output of the EKF of the autopilot mounted on the Penguin-B. An exact reference for the gyro bias is not available, but an approximation of it is calculated by averaging the gyro measurements at standstill before the flight. The accelerometer bias is not estimated, but it is computed the same way as the gyro bias and subtracted from the accelerometers measurements before they are used in the observer.

The results presented here refer to a complete flight of the Penguin-B, from take-off to landing, corresponding to a travelled distance of approximately 9 km in around 5 min. The time on the x-axes is the elapsed time since the data logging begins, and only the significant part involving the flight is represented. The manoeuvres performed include flights on a straight line and turns with a large and small radius of curvature, namely approximately 200 m and 100 m; the trajectory described is depicted in Fig. 3. The UAV was operated manually during take-off and landing, while it flew automatically otherwise, following predetermined waypoints.

B. Results

Three different case studies are considered here, depending on how the roll and pitch angles are obtained: from accelerometers, from inclinometers, and from $\hat{R}$. The estimation errors are presented in Fig. 4–7. The position and velocity errors all reach zero and present no significant differences, as expected when the GPS is always available. The attitude errors have instead different behaviours: when using roll and pitch from accelerometers, the performance is clearly worse than the other two cases. The roll and pitch estimates are slightly better when using feedback from $\hat{R}$ than when using inclinometers, whereas the yaw estimate often has the opposite outcome. The gyro bias error is more erratic: around the x-axis, the estimates are best with accelerometers and worst with inclinometers;
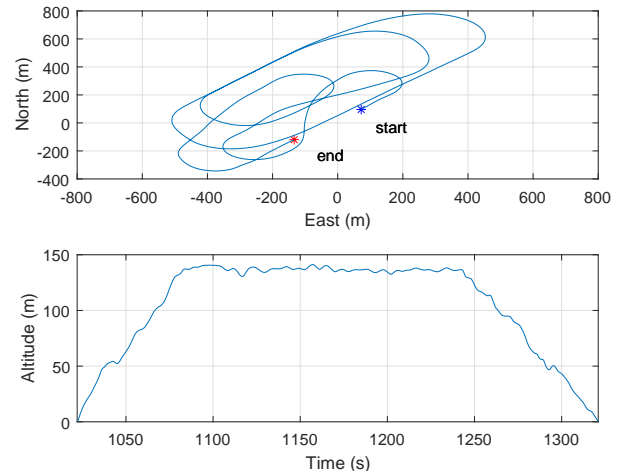

Fig. 3. Position on the N-E plane and altitude, as output by the EKF, used as reference. The blue and red stars indicate the start and end of the data set, respectively.
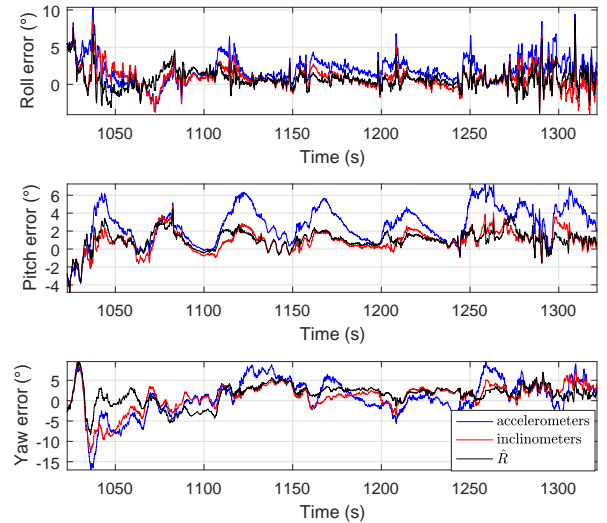

Fig. 4. A comparison of the attitude error from the three methods.

around the y-axis, the case with $\hat{R}$ is the best one, with inclinometers behaving slightly worse and the accelerometers quite bad; around the z-axis, all three cases present similar results, but the case with $\hat{R}$ looks more precise and accurate. The most probable reason for this is that an exact reference for the gyro bias is not available; what is used is the value measured at standstill before the flight, but it would certainly vary during the flight. As the reference is not very accurate–but it is the best avaialble–the estimation error for the gyro bias is the least significant term of comparison to decide which method performs best. The estimated gyro bias has, however, a significant impact on the estimated attitude: as this is worse with accelerometers than with inclinometers or $\hat{R}$, it can be stated that $\hat{R}$ yields the most accurate overall results.

A key assumption is that all image features have zero altitude: this can be too strict and unrealistic in many cases, but the results presented here indicate that the estimation errors
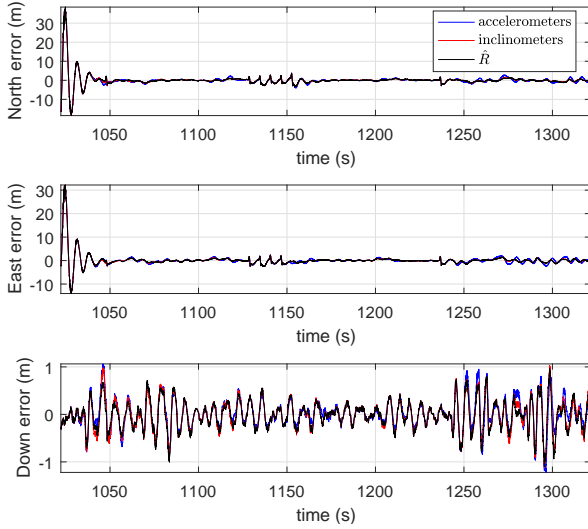
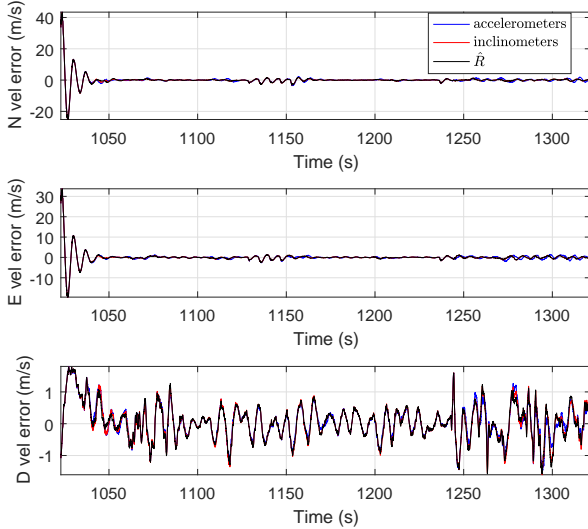Fig. 5. A comparison of the NED position error from the three methods.

Fig. 6. A comparison of the NED velocity error from the three methods.
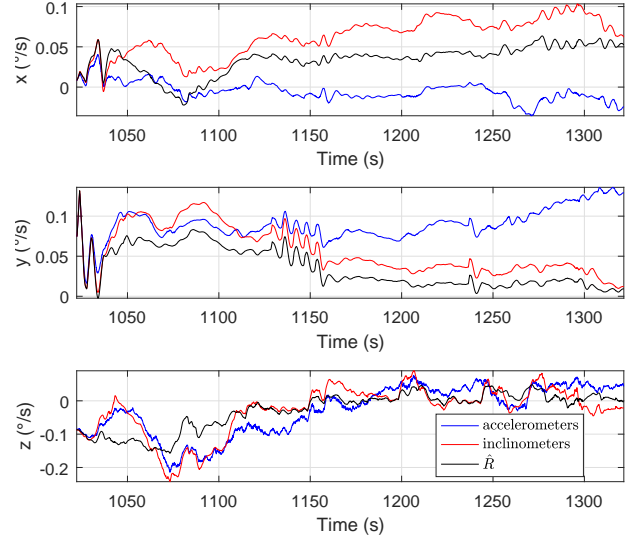

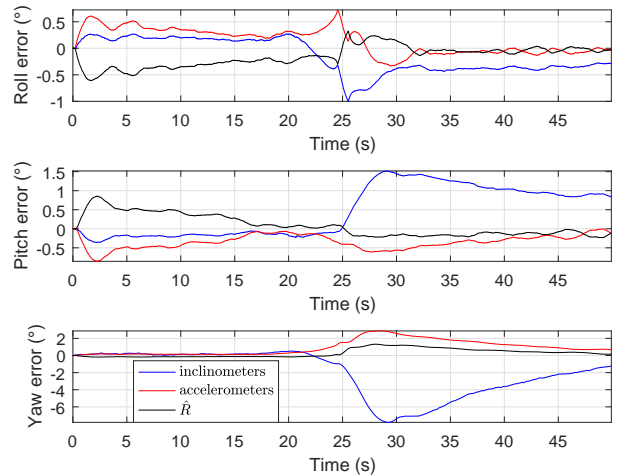Fig. 7. A comparison of the gyro bias deviation from reference from the three methods.

Fig. 8. Attitude errors resulting from the simulation. The flight path features a straight line, a sharp turn by $180°$ with radius of curvature 40 m, and another straight line. The turn begins at time 24 s.

are not large enough to require a more accurate terrain model for this experiment.

VI. SIMULATION RESULTS

The solution with inclinometers is supposed to provide less accurate estimates than the case with $\hat{R}$ in manoeuvres characterized by high accelerations, like sharp turns, so it is worth checking the behaviour of the attitude observer in such occasions. The estimation error in Fig. 4 is always very small, so it is reasonable to wonder whether the reference values used here, i.e. the EKF of the autopilot, are really the closest to the real values. The solution is to test the observer on simulated data, for which the reference values are perfectly known.

The simulator is similar to the one in [27], with the following differences. The UAV path is composed of a straight line, a sharp turn by $180°$ with radius of curvature 40 m, and

a final straight line. The flight is simulated over flat terrain, white noise is added to all measurements and it is assumed that the UAV has flown long enough to let the gyro bias estimation error be zero. A model for the inclinometer is taken from [36], where the authors proposed a model of the U.S. Digital T2-7200-T optical inclinometer and identified its parameters.

Fig. 8 shows the Euler angles estimation errors for the simulation. The sharp turn begins at time 24 s, and it is evident that the case with feedback from $\hat{R}$ performs better than the ones with inclinometers or accelerometers. This is not a surprise: as explained in Sec. III-C, roll and pitch measurements based on inclinometers or accelerometers are solutions that suffer from known problems in the presence of large accelerations. Inclinometers perform worse than accelerometers, but this depends on what type of models are considered.

VII. Conclusions

In this paper two non-linear observers for navigation of a UAV were analysed and tested. The sensors used were an altimeter, a GNSS receiver, an IMU, and a camera. Also roll and pitch were necessary, and the difference between the two observers was in how such angles were obtained. The first observer made use of roll and pitch measurements from sensors, i.e. inclinometers or accelerometers, in the machine vision system in order to provide the body-fixed velocity of the UAV, and it was proven to be GES. The replacement of the roll and pitch measurements with the feedback from $\hat{R}$ gave rise to a slightly different observer, which required a new analysis and was proven to be ULES. The paper also provided a description of the machine vision system employed, how the OF was calculated, and how it could be used to obtain the body-fixed velocity. Both observers were then tested on experimental data, which confirmed the theoretical results.

Acknowledgment

References

[1] P. Batista, C. Silvestre, and P. Oliveira, "GES attitude observers - Part I: Multiple general vector observations," *Proc. of the 18th IFAC World Congress*, vol. 18, pp. 2985–2990, 2011.

[2] ——, "GES attitude observers - Part II: Single vector observations," *Proc. of the 18th IFAC World Congress*, vol. 18, pp. 2991–2996, 2011.

[3] H. F. Grip, T. I. Fossen, T. A. Johansen, and A. Saberi, "Attitude estimation using biased gyro and vector measurements with time-varying reference vectors," *IEEE Transactions on Automatic Control*, vol. 57, no. 5, pp. 1332–1338, 2012.

[4] J. Guerrero-Castellanos, H. Madrigal-Sastre, S. Durand, L. Torres, and G. Muoz-Hernndez, "A robust nonlinear observer for real-time attitude estimation using low-cost MEMS inertial sensors," *Sensors*, vol. 13, no. 11, pp. 15 138–15 158, 2013.

[5] M. D. Hua, G. Ducard, T. Hamel, R. Mahony, and K. Rudin, "Implementation of a nonlinear attitude estimator for aerial robotic vehicles," *IEEE Trans. Control System Technol.*, vol. 22, no. 1, pp. 201–213, 2014.

[6] M. D. Hua, T. Hamel, R. Mahony, and J. Trumpf, "Gradient-like observer design on the special euclidean group se(3) with system outputs on the real projective space," *Proceedings of the 54th IEEE Conference on Decision and Control (CDC)*, pp. 2139–2145, 2015.

[7] M. D. Hua, P. Martin, and T. Hamel, "Stability analysis of velocity-aided attitude observers for accelerated vehicles," *Automatica*, vol. 63, pp. 11–15, 2016.

[8] R. Mahony, T. Hamel, and J. M. Pflimlin, "Nonlinear complementary filters on the special orthogonal group," *IEEE Transactions on Automatic Control*, vol. 53, no. 5, pp. 1203–1218, 2008.

[9] R. Mahony, T. Hamel, J. Trumpf, and C. Lageman, "Nonlinear attitude observers on SO(3) for complementary and compatible measurements: A theoretical study," *Proceedings of the 48th IEEE Conference on Decision and Control*, pp. 6407–6412, 2009.

[10] R. Mahony, M. Euston, J. Kim, P. Coote1, and T. Hamel, "A non-linear observer for attitude estimation of a fixed-wing unmanned aerial vehicle without GPS measurements," *Transactions of the Institute of Measurement and Control*, vol. 33, no. 6, pp. 699–717, 2011.

[11] J. Trumpf, R. Mahony, T. Hamel, and C. Lageman, "Analysis of non-linear attitude observers for time-varying reference measurements," *IEEE Trans. Autom. Control*, vol. 57, no. 11, pp. 2789–2800, 2012.

[12] S. Salcudean, "A globally convergent angular velocity observer for rigid body motion," *IEEE Transactions on Automatic Control*, vol. 36, no. 12, pp. 1493–1497, 1991.

[13] J. Thienel and R. M. Sanner, "A coupled nonlinear spacecraft attitude controller and observer with an unknown constant gyro bias and gyro noise," *IEEE Transactions on Automatic Control*, vol. 48, no. 11, pp. 2011–2015, 2003.

[14] M. D. Hua, "Attitude estimation for accelerated vehicles using GPS/INS measurements," *Control Engineering Practice*, vol. 18, no. 7, pp. 723–732, 2010.

[15] H. F. Grip, T. I. Fossen, T. A. Johansen, and A. Saberi, "A nonlinear observer for integration of GNSS and IMU measurements with gyro bias estimation," *American Control Conference*, pp. 4607–4612, 2012.

[16] ——, "Globally exponentially stable attitude and gyro bias estimation with application to GNSS/INS integration," *Automatica*, vol. 51, pp. 158–166, 2015.

[17] ——, "Nonlinear observer for GNSS-aided inertial navigation with quaternion-based attitude estimation," *American Control Conference*, pp. 272–279, 2013.

[18] B.Lucas and T.Kanade, "An iterative image restoration technique with an application to stereo vision," *Proc. DARPA Image Underst, Workshop*, pp. 121–130, 1981.

[19] B.K.P.Horn and B.G.Schunk, "Determining optical flow," *Artif. Intell.*, vol. 17, pp. 185–204, 1981.

[20] D. Lowe, "Object recognition from local scale-invariant features," *Proc. Int. Conf. Computer Vision*, pp. 1150–1157, 1999.

[21] H. Bay, A. Ess, T. Tuytelaars, and L. Van Gool, "Speeded-up robust features (surf)," *Computer vision and image understanding*, vol. 110, no. 3, pp. 346–359, 2008.

[22] A. Shabayek, C. Demonceaux, O. Morel, and D. Fofi, "Vision based uav attitude estimation: Progress and insights," *Journal of Intelligent and Robotic Systems: Theory and Applications*, vol. 65, no. 1-4, pp. 295–308, 2012.

[23] M. Mammarella, G. Campa, M. L. Fravolini, and M. R. Napolitano, "Comparing optical flow algorithms using 6-dof motion of real-world rigid objects," *IEEE Trans. on Systems, Man, and Cybernetics, Part C: Applications and Reviews*, vol. 42, no. 6, pp. 1752 – 1762, 2012.

[24] H. Chao, Y. Gu, and M. Napolitano, "A survey of optical flow techniques for robotics navigation applications," *Journal of Intelligent and Robotic Systems: Theory and Applications*, vol. 73, no. 1-4, pp. 361–372, 2014.

[25] L. Fusini, T. I. Fossen, and T. A. Johansen, "A uniformly semiglobally exponentially stable nonlinear observer for GNSS- and camera-aided inertial navigation," *22nd Mediterranean Conf. Control and Automation*, pp. 1031–1036, 2014.

[26] L. Fusini, T. A. Johansen, and T. I. Fossen, "Experimental validation of a uniformly semi-globally exponentially stable non-linear observer for gnss- and camera-aided inertial navigation for fixed-wing uavs," *Proc. Int. Conf. Unmanned Aircraft Syst.*, 2015.

[27] J. Hosen, H. H. Helgesen, L. Fusini, T. I. Fossen, and T. A. Johansen, "A vision-aided nonlinear observer for fixed-wing UAV navigation," *Proc. of the AIAA Guidance, Navigation, and Control Conference*, 2016.

[28] H. F. Grip, A. Saberi, and T. A. Johansen, "Observers for interconnected nonlinear and linear systems," *Automatica*, vol. 48, no. 7, pp. 1339–1346, 2012.

[29] H. K. Khalil, *Nonlinear systems*, 3rd ed. Upper Saddle River, NJ: Prentice-Hall, 2002.

[30] T. I. Fossen, *Handbook of Marine Craft Hydrodynamics and Motion Control*. Chichester, UK: John Wiley & Sons, Ltd, 2011.

[31] M. D. Shuster and S. D. Oh, "Three-axis attitude determination from vector observations," *Journal of Guidance, Control and Dynamics*, vol. 4, no. 1, pp. 70–77, 1981.

[32] S. Del Pizzo, S. Troisi, A. Angrisano, and S. Gaglione, "Roll and pitch estimation using visual horizon recognition," in *Augmented and Virtual Reality*. Springer International Publishing, 2014, pp. 363–380.

[33] R. W. Beard and T. W. McLain, *Small Unmanned Aircraft: Theory and Practice*. Princeton, NJ: Princeton University Press, 2012.

[34] G. Stewart, "Stochastic perturbation theory," *SIAM Review*, vol. 32, no. 4, pp. 579–610, 1990.

[35] G. Bradski, "The opencv library," *Doctor Dobbs Journal*, vol. 25, no. 11, pp. 120–126, 2000.

[36] J. Leavitt, A. Sideris, and J. E. Bobrow, "High bandwidth tilt measurement using low-cost sensors," *IEEE/ASME Transactions on Mechatronics*, vol. 11, no. 3, pp. 320–327, 2006.